Acta Biomaterialia 106 (2020) 242–255

Contents lists available at ScienceDirect

Acta Biomaterialia

journal homepage: www.elsevier.com/locate/actbio

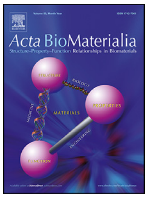

Full length article

Contributions of intermolecular bonding and lubrication to the mechanical behavior of a natural armor

H. Jiang[a,b], S. Ghods[b], E. Weller[b], S. Waddell[b], E.A. Ossa[c], F. Yang[a], D. Arola[b,d,e,*]

[a] Jiangsu Key Laboratory of Engineering Mechanics, School of Civil Engineering, Southeast University, Nanjing, JS, China
[b] Department of Materials Science and Engineering, University of Washington, Roberts Hall, 333, Box 352120, Seattle, WA 98195-2120, USA
[c] School of Engineering, Universidad EAFIT, Medellín, Colombia
[d] Department of Mechanical Engineering, University of Washington Seattle, WA USA
[e] Department of Mechanics, Shanghai University, Shanghai, China

ARTICLE INFO

Article history:
Received 25 August 2019
Revised 10 February 2020
Accepted 11 February 2020
Available online 19 February 2020

Keywords:
Fish scales
Interpeptide bonding
Lubrication
Natural armor
Toughness
Apparent Poisson's ratio

ABSTRACT

Among many dermal armors, fish scales have become a source of inspiration in the pursuit of "next-generation" structural materials. Although fish scales function in a hydrated environment, the role of water and intermolecular hydrogen bonding to their unique structural behavior has not been elucidated. Water molecules reside within and adjacent to the interpeptide locations of the collagen fibrils of the elasmodine and provide lubrication to the protein molecules during deformation. We evaluated the contributions of this lubrication and the intermolecular bonding to the mechanical behavior of elasmodine scales from the Black Carp (*Mylopharyngodon piceus*). Scales were exposed to polar solvents, followed by axial loading to failure and the deformation mechanisms were characterized via optical mechanics. Displacement of intermolecular water molecules by liquid polar solvents caused significant ($p \leq 0.05$) increases in stiffness, strength and toughness of the scales. Removal of this lubrication decreased the capacity for non-linear deformation and toughness, which results from the increased resistance to fibril rotations and sliding caused by molecular friction. The intermolecular lubrication is a key component of the "protecto-flexibility" of scales and these natural armors as a system; it can serve as an important component of biomimetic-driven designs for flexible armor systems.

Statement of Significance

The natural armor of fish has become a topic of substantial scientific interest. Hydration is important to these materials as water molecules reside within the interpeptide locations of the collagen fibrils of the elasmodine and provide lubrication to the protein molecules during deformation. We explored the opportunity for tuning the mechanical behavior of scales as a model for next-generation engineering materials by adjusting the extent of hydrogen bonding with polar solvents and the corresponding interpeptide molecular lubrication. Removal of this lubrication decreased the capacity for non-linear deformation and toughness due to an increase in resistance to fibril rotations and sliding as imparted by molecular friction. We show that intermolecular lubrication is a key component of the "protecto-flexibility" of natural armors and it is an essential element of biomimetic approaches to develop flexible armor systems.

1. Introduction

Endowed with toughness and flexibility, modern fish scales are key components of the natural armors of most fish. The primary function of this armor is to protect the fish from external physical threats without interfering with locomotion. Fish scales exhibit large variations in size, shape and arrangement, ranging from the microscopic scales of sharks and rays, to the stiff and strong ar-

---

[*] Corresponding author at: Department of Materials Science and Engineering, University of Washington, Roberts Hall, 333, Box 352120, Seattle, WA 98195-2120, USA.

E-mail address: darola@uw.edu (D. Arola).

https://doi.org/10.1016/j.actbio.2020.02.014

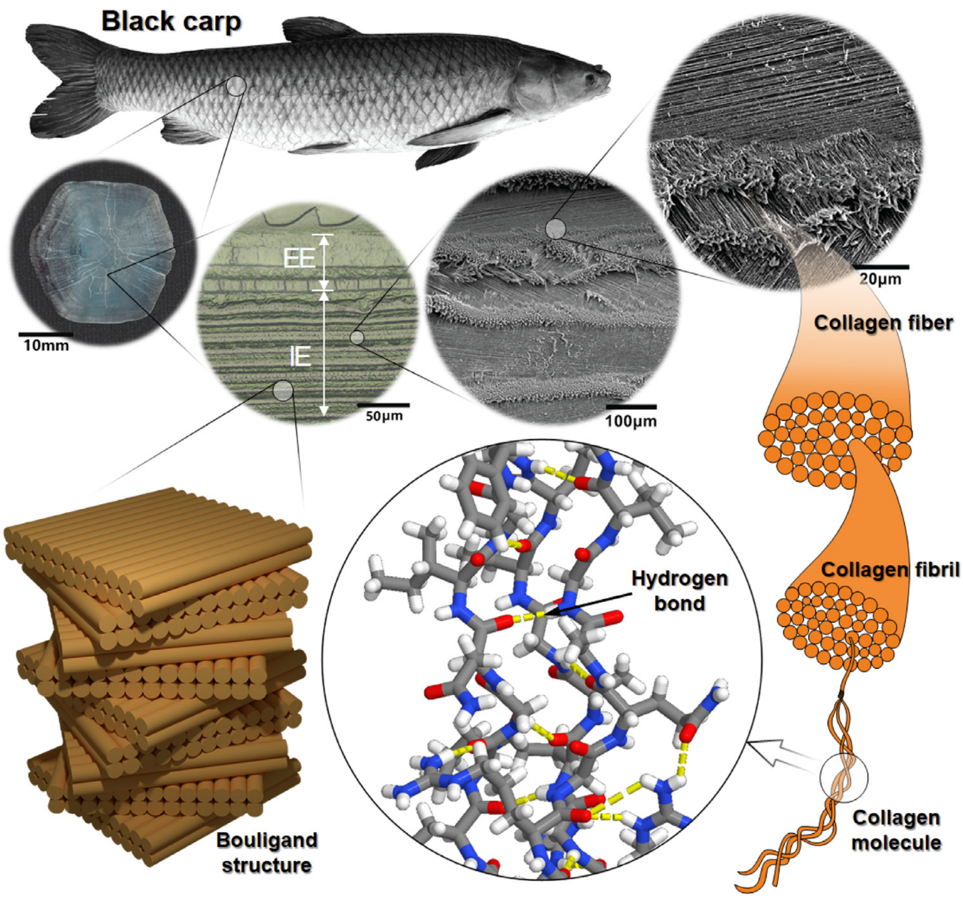

Fig. 1. Hierarchical structure of fish scales from the black carp from the macro- to the nano-scale. The aspect of scale structure explored in this investigation is the interpeptide hydrogen bonding and its importance to fibril deformation, including contributions from the interpeptide liquid on fibril sliding.

mor plates of bichirs and sturgeon. The general classification of fish scales in modern fish includes cosmoid, elasmoid, ganoid, and placoid scales [1,2]. Elasmoid scales are thin and highly flexible. They are generally found on fish with greater swim speeds. Scales of the other three classes are relatively stiff and becoming less common in the species of today [3].

Elasmoid scales consist of type I collagen fibers reinforced by apatite mineral platelets. In comparison to hard tissues like dentin and bone, which exhibit mineral content over 60% by weight, the mineralization of elasmoid scales is much lower and exhibits strong spatial gradients [4–6]. According to the relative extent of mineralization, elasmoid scales have three distinct layers. The outermost limiting layer (LL) is highly mineralized and serves as the first barrier against penetration [1]. The mineralization extends from the LL into the underlying elasmodine, which consists of plies of uniaxial collagen fibers. According to its mineral content, the elasmodine has two layers. The outer and more highly mineralized layer is the external elasmodine (EE), while the internal elasmodine (IE) is closest to the fish body (Fig. 1) [6]. Collagen fibrils of the EE are sparsely reinforced with nano-crystals of apatite, similar to that in bone and dentin, whereas the mineral content of the IE is negligible [7]. The fibrils are formed through self-assembly of collagen molecules using coordinated hydrogen bonds [8–11] and are bundled into fibers with a thin layer of interfibrillar protein matrix [12].

The plies of uniaxial collagen fibrils of the EE and IE are organized with a so-called “plywood-like” stacking arrangement, which is regarded as a Bouligand structure [13]. The angles between fibrils in these plies have been reported to vary from 36° to 90° depending on species [14–18]. Murcia et al. [17] showed that the scales from carp and tarpon possess a relative rotation of 75° between adjacent plies, with some variability, whereas arapaima scales have a relative rotation closer to 90°. The ply thickness depends on the fish species, with general range between 10 and 50 μm [17].

Such sophisticated microstructure and mineral distribution bestow elasmoid scales with unique mechanical properties. The highly mineralized LL provides the initial resistance to puncture. By virtue of its stiffness, it distributes the load transmitted onto the elasmodine over a large area [1]. The elasmodine provides flexibility and toughness to the scales, and can undergo significant deformation to resist failure [19]. Nature uses this compliant “backing layer” to resist penetration. An overly flexible layer could permit contusion damage to the underlying tissues. The Bouligand lamination structure of the elasmodine adapts to loads by reorienting the collagen fibril plies [15,20], which reduces stiffness and enhances the fracture resistance as well. As such, the collagen layer assists in providing flexibility and arresting damage.

Understanding the arrangement of building blocks in natural materials, as well as the deformation/failure mechanisms they bestow, is a prerequisite for designing biomimetic materials [21–23]. Numerical simulations and carefully-designed experiments are two approaches for determining how natural materials can possess superior qualities despite the relatively inferior mechanical properties of their constituents [24,25]. Through computational simulation, Vernerey et al. [26] showed that scale rotations induce a softer bending stiffness in the longitudinal direction of the fish body that preserves the freedom of motion (i.e., armor flexibility). Murcia et al. [27] demonstrated that the elastic modulus, strength and modulus of toughness of elasmoid scales from the carp could be increased over 100% by chemical dehydration; the increase in elastic modulus of scales from the tail region exceeded 200%, which was attributed to the lower mineral content. The changes in mechanical properties were attributed to increases in the degree of interpeptide hydrogen bonding of collagen molecules, whereas the spatial variations were associated with differences in the degree of mineralization across anatomical sites.

In situ measurement methods are helpful to assess important mechanistic contributions to the mechanical behavior of natural materials. For example, Zimmermann et al. [20] applied *in situ* synchrotron small-angle X-ray scattering to *Arapaima gigas* scales during stretching and characterized the nano-micro deformation mechanisms derived from the Bouligand structure. Here, we investigate the micro-meso mechanisms of deformation in scales of the Black Carp and the contributions of intermolecular lubrication and bonding through *in situ* experiments involving digital image correlation. The role of water as an aid to interfibrillar sliding and lubrication is explored and its importance to the "protecto-flexibility" aspect of individual scales is discussed.

2. Materials and methods

2.1. Materials

A black carp (*M. piceus*) was purchased from a commercial vender with weight and length of 7 kg and 95 cm, respectively. The age of this fish was approximately 4 years old, implying it had reached sexual maturity. The scales were extracted from the fish using tweezers in two regions including adjacent to the head and near the tail. They corresponded to distances defined along the lateral line from the gill plate to the tail of 15% and 80% of the total number of scales, respectively. The scales in these two regions were symmetrically removed between the dorsal and ventral aspects, on opposite sides of the lateral line of the body. The thickness of the scales was less than 1 mm and the effective diameter varied depending on the anatomical position. Scales from the head region possessed a diameter of roughly 30 mm, while those from the tail region were less than 25 mm. All of the scales had an effective diameter greater than 15 mm. After their removal, the scales were placed in a Hanks Balanced Salt Solution (HBSS) bath and stored at −20 °C to minimize the possibility of degradation until testing. In advance of sample preparation and testing, the scales were thawed in HBSS at 3–5 °C for 30 min.

Conventional dog-bone shaped specimens were sectioned from the scales using a punch and stamping process consistent with our previous study [7]. The specimens had a gage-section width and length of 2 mm and 7.5 mm, respectively, and a total length of 14.5 mm as shown in Fig. 2a. All specimens were stamped from the center of the scale, which is the region with most uniform thickness. The specimens were obtained with an orientation that is parallel to the lateral line of the body. Previous studies have shown that the IE of elasmoid scales has in-plane isotropic mechanical properties [1,18]. Nevertheless, potential changes in this behavior induced by the polar solvents warranted consistency in the methods of preparation. To obtain samples limited to the IE of the scales, it was gently separated from the stamped full scale specimens under hydration using a dissection needle, as shown in Fig. 2b. The IE of the scales were evaluated to remove the influence of the highly mineralized limiting layer and external elasmodine, which would have much different influence from the polar solvent treatments due to the interference of the mineral.

After separation of the LL and EE, the IE specimens were soaked in a polar solvent of either HBSS, methanol, ethanol, or acetone at 3–5 °C for 48 h. That insured that there were no dimensional changes occurring to the scales (e.g., shrinking) while they were undergoing uniaxial tension. The polarity of these solvents can be described according to either Hansen's or Hoy's solubility parameters for hydrogen bonding, the latter being more common. According to Hoy's triple solubility parameter model, the solubility parameter for hydrogen bonding forces (δ_h) for HBSS, methanol, ethanol and acetone are 40.4, 24.0, 20.0, and 11.0 MPa$^{1/2}$, respectively [28]. An additional group of samples were maintained in air (relative humidity ≈ 25%) at room temperature for 48 h. The value of δ_h for interpeptide hydrogen bonds within collagen fibrils in air has been estimated as 14.8 MPa$^{1/2}$ [28]. To prevent the samples from distorting during dehydration they were sandwiched between two glass slides. That ensured that the samples were flat after exposure to the polar solvents and that they would not undergo out-of-plane bending during the tensile tests as a result of inherent curvature. This process of restraining the specimen distortion could introduce a residual stress into the fish scale samples. However, due to the low elastic modulus of the IE = ($0.2 \leq E \leq 3$ GPa), the magnitude of this residual stress would be small. In addition, there is no further contribution of the residual stresses to the mechanical behavior after the onset of inelastic deformation, which was the predominant aspect of the scale responses evaluated. Therefore, its contribution to the mechanical behavior was neglected. Five specimens were evaluated for each of the five treatment conditions (HBSS, methanol, ethanol, acetone and air) and from each anatomical region (head and tail). Consequently, a total of 50 specimens were prepared and evaluated within the core of this evaluation. Additional samples were evaluated as a part of pilot testing and to validate the experimental methods.

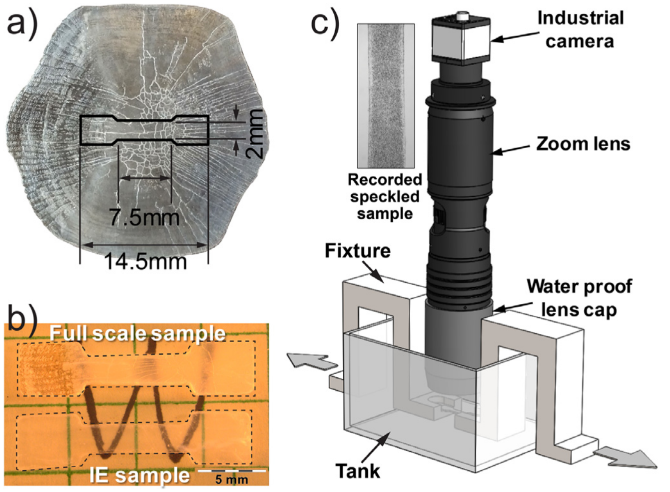

Fig. 2. Details of the experimental methods to evaluate the mechanical behavior of the scales. (a) A single specimen is sectioned from the center of a scale with an orientation parallel to the lateral line axis of the fish body. The dimensions of the specimens are noted. (b) Specimens consisting of the full-scale thickness (LL, EE and IE) and only the IE after peeling away the highly mineralized layers. Note that the IE specimen is partly transparent. (c) Schematic diagram of the 2D-DIC system used to evaluate the full-field deformation in the samples while submerged in a solvent tank. The tank is filled with the desired solvent and the water proof lens cap is introduced below the liquid level.

2.2. Tensile testing

The tensile testing was performed using a commercial horizontal universal testing machine (Yuansheng Tech, Microtensile Tensile Tester, Shanghai China) equipped with a 200 N load cell, and with load precision of 0.03%. The fixture shape offered space for a container, which was used to immerse the specimens in polar solvents during testing and facilitate application of optical imaging. Tensile testing of the IE specimens was performed within the appropriate solvent bath to failure at room temperature. A set of specially designed fixtures were fabricated from stainless steel to enable the tensile testing as shown in Fig. 2c. The loading was performed using a stroke rate of 0.5 mm/min under displacement control, which corresponded to a strain rate of approximately 1×10^{-3} s^{-1} according to the specimen gage length. A preload of 0.2 N was applied to the specimens as part of the loading process to minimize out-of-plane deformation of the compliant specimens and facilitate the application of Digital Image Correlation (DIC). The load was acquired as a function of time, and the in-plane displacement and strain were acquired using DIC as detailed in Section 2.3. To validate the methods of tensile testing applied to the scales, they were also used for evaluating a control material (polycarbonate (PC)). The mechanical properties estimated from tensile responses of the PC control included the yield and ultimate strengths of approximately 50 and 78 MPa, respectively, and the elastic modulus of 2.6 GPa. Most importantly, the average Poisson's ratio obtained from the elastic range of the tensile tests was 0.3, which is very consistent with the reported values from multiple studies [55–58] and validated the methods of evaluation.

The synchronized stress–strain responses acquired from tensile testing were used to determine the elastic modulus (E), strength (S), strain to failure (FS) and modulus of toughness (MOT) using the engineering stress–strain definitions as highlighted in Fig. 3b. These metrics were calculated for all of the specimens tested to characterize the contributions of the solvents to the mechanical behavior. The elastic modulus was determined using a tangent method for strains less than 1%; the strength and strain to failure was defined by the maximum stress and strain realized by the sample, respectively; the MOT was calculated by integrating the area under the stress–strain curves as a function of strain until failure. The MOT quantifies the ability of a material to dissipate energy to failure through inelastic deformation. It is not a measure of fracture toughness, which is a measure of a materials resistance to the growth of a crack and involves the energy required to develop new surface area. While both the MOT and fracture toughness contribute to the puncture resistance, the former is more important to the IE, based on the contribution of its capacity for inelastic deformation to the overall puncture resistance of scales [1].

There are alternatives to tensile testing that were considered for evaluating the mechanical behavior of the scales. Nanoindentation and acoustic methods (i.e., ultrasound) are potent candidates for evaluating the elastic properties of materials. There are difficulties that reduce the applicability of these techniques in the present investigation. *In situ* evaluation of the scales within the polar solvent bath complicates the application of nanoindentation. Evaporation of the solvents during the indentions, as well as the more extensive sample preparation to achieve the required surface roughness and flatness are two difficulties associated with nanoindentation. Considering the use of ultrasound, it is most promising for homogeneous materials and considered valid for heterogeneous materials, when the wavelength is large compared to any characteristic length of the material [29]. While those hardships can be overcome, the layered nature of the IE specimens and their very small thickness ($\ll$1 mm) reduces confidence in the measurements. However, the primary limitation of the aforementioned techniques is that they are not capable of quantifying many of the properties of interest, namely strength, strain to fracture and toughness. Therefore, they were not adopted for this investigation.

2.3. 2D-DIC

Optical methods, such as electronic speckle pattern interferometry (ESPI) [30,31] and DIC [32,33] are attractive full-field measurement techniques [34,35] for assisting in characterizing the structural behavior of materials over finite areas of evaluation. Due to the relatively large strain to failure of the fish scales, DIC is the only optical technique that enables characterization over the entire gage-section and through the entire range of deformation. Two-dimensional DIC (2D-DIC) was used to map the full-field strain distribution in the samples during testing. Sequential images documenting the deformation process were acquired using an industrial monochrome camera (CMOS, UI-3180CP-M-GL, IDS, Obersulm, Germany) with resolution of 2592 × 2048 pixels. The camera was equipped with a micro-inspection lens (Optem Zoom 70XL, Thales Optem Inc., Fairport, NY, USA), as shown in Fig. 2c. The image acquisition rate was 1 frame per second and the field of view (FOV) was 8 mm × 6 mm, which covered the entire gage section. A custom water-proof cup was mounted on the lens to enable image acquisition within the liquid bath and a standard dual gooseneck microscope illuminator was used for enhancing illumination. To facilitate the application of DIC, a speckle distribution was deposited on the viewing surface of the specimens using a multi-purpose airbrush with a 0.2 mm needle/nozzle. The speckles were created using toner powder, which consisted of black particles. The powder did not contain any solvents.

Calculation of the strain field within the gage section of the specimens was performed with the acquired optical images using a commercial software (PMLAB DIC-3D, Nanjing PMLAB Sensor Tech Co., Ltd., Nanjing, China). Details regarding 2D-DIC and some relevant applications are described elsewhere [36–38]. The evolution in axial strain within the gage section of an IE specimen and over the whole loading period is presented in Fig. 3a.

The axial and transverse strain distributions were determined from the corresponding deformation fields. The apparent Poisson's ratio *APR* was determined from the strain maps and the ratio in mean strains in the transverse e_{yy} and axial direction e_{xx} according to $APR = -e_{xx}/e_{yy}$. Note that for small strains and within the elastic range, the APR is the Poisson's ratio of the material. Beyond the elastic range it was unclear if volume was conserved and over what extent of strain. Thus, APR is a suitable manner to describe the strain ratio. The evolution in APR with tensile loading was documented as a function of the axial strain to failure.

The tensile specimens were stamped from individual fish scales, which can introduce challenges that are not encountered in characterizing the properties of engineering materials. Special care was taken during the specimen preparation and testing process to ensure that the specimens were flat and that the stress distribution resulting from the tensile testing was uniaxial. The axial displacement and strain maps obtained from DIC served as an effective means of monitoring these important aspects of the specimens and their quality. In particular, the deformation field was used to confirm that the specimens were aligned with the longitudinal axis and the corresponding strain fields were used to confirm that there was no curvature or deviation in specimen flatness.

2.4. Statistical analysis

All of the mechanical property measurements obtained from the tensile tests involved replication, Specifically, five specimens were obtained from five different scales that were obtained at each location, which supported a determination of the mean ± standard deviation of the properties. In comparing the experimental values for the PC control with reported values, the error was estimated from the difference. The mechanical properties of the IE specimens were compared in terms of location (head vs. tail) and polar solvent polarity (Hoy's solubility parameter) using a two-way ANOVA with significant differences identified by $p \leq 0.05$. The data was assessed prior to application of the ANOVA to confirm that it met the assumptions of homoskedasticity and normality. The statistical analysis was performed with OriginPro 2018 software

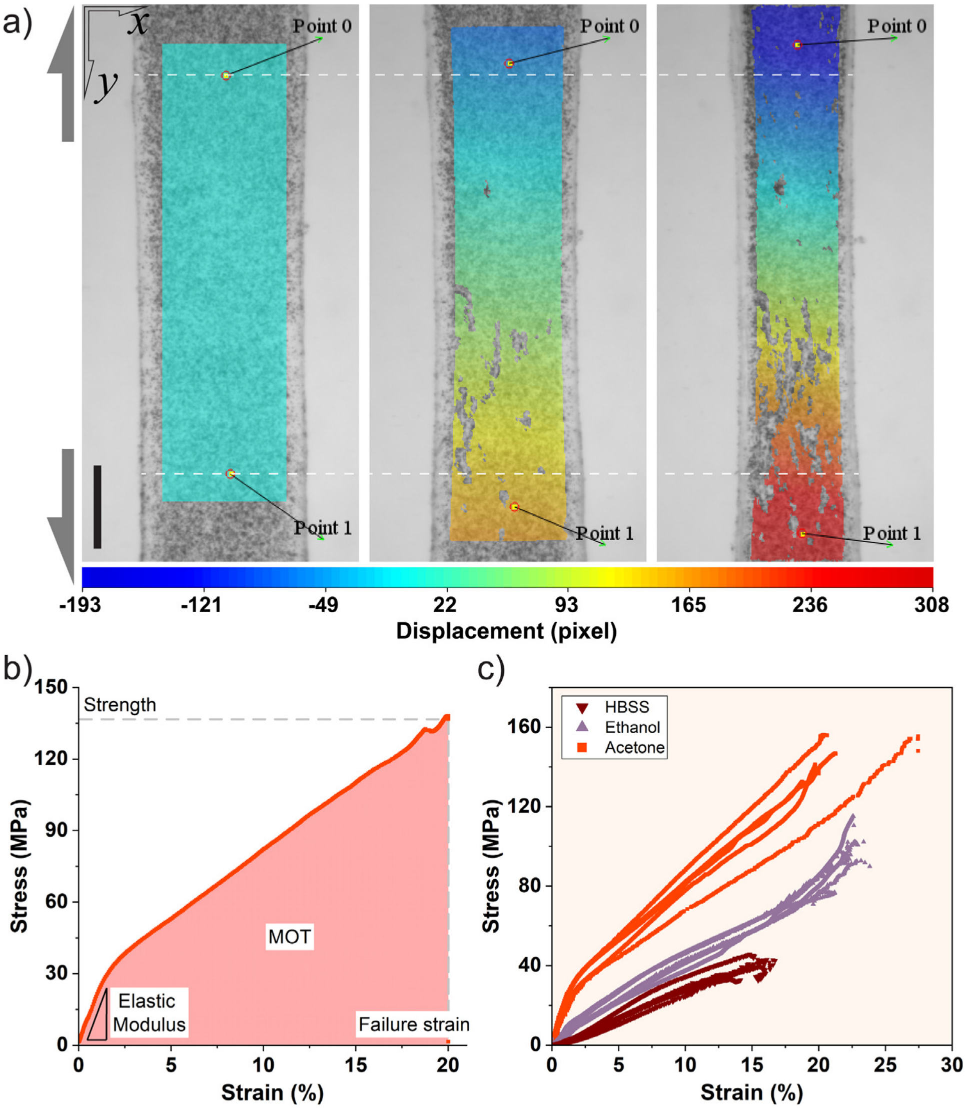

Fig. 3. Determination of the engineering stress–strain responses using the full-field displacement maps obtained by 2D-DIC and the evaluation of mechanical properties. (a) Displacement maps for an IE specimen for axial loading (y-direction). Shown are the initial positions (left), intermediate loading (middle) and near failure (right). The distance between Points 0 and 1 of the gage section are used to calculate the axial strain. Scale bar = 1 mm. (b) The engineering stress–strain response for an IE specimen exposed to acetone and definitions of the measured properties. (c) Stress–strain responses for multiple IE specimens exposed to three different solvents. Note the large degree of consistency.

(OriginLab Corp., MA, USA) at a confidence level of 95%, which is typical in structural evaluations.

3. Results

A representative stress–strain curve obtained from tensile testing of an IE specimen to failure within acetone is shown in Fig. 3b. The mechanical properties obtained from these responses are highlighted in this figure for clarity. A comparison of stress–strain curves for specimens obtained from multiple scales of the head region and treated using HBSS, ethanol, and acetone is shown in Fig. 3c. As evident from the distribution of the curves, the solvent treatments imposed substantial effects on the tensile responses. The elastic modulus and strength within acetone reach values nearly 30x and 4x greater, respectively than those properties within in HBSS. Also evident in Fig. 3c, the stress–strain curves for the family of specimens evaluated in each condition are quite consistent. Nevertheless, there is some variability that is important to consider in quantifying the responses and in assessing the statistical differences in the responses.

Fig. 4 presents comparisons of the stress–strain responses for the IE specimens across all of the five different treatments. These are stochastic representations describing the moving average and standard deviation of responses from the five tensile specimens of each group. Results for specimens obtained from scales of the head and tail regions are shown in Fig. 4a and b, respectively. As evident from these curves, the stress–strain responses for specimens from the head and tail regions are almost identical. The relative stiffness and strengths of those specimens exposed to solvents are inversely distributed with respect to the polarity (i.e., solubility parameters). The solvent polarity is ordered from highest to lowest from HBSS, methanol, ethanol and acetone. As such, there is a decrease in the elastic modulus and strength with increasing polarity of the aqueous environment. Apart from the partial overlap of responses for the ethanol and methanol treatments, results for the other treatments are significantly different ($p \leq 0.05$).

The stress–strain curves in Fig. 4 for the specimens exposed to ethanol, methanol and HBSS are nearly linear to failure. In comparison, the acetone-treated and air-dried specimens exhibit bi-linear distributions with distinct linear elastic portion, followed by a sec-

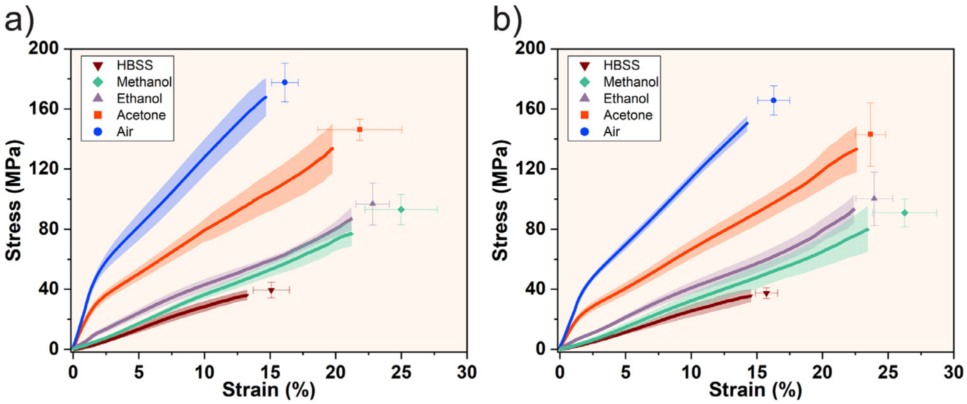

Fig. 4. Engineering stress–strain responses for specimens obtained from the IE of scales and after the five different polar solvent treatments. The data is shown in terms of the moving average and standard deviation of the responses obtained from all scales evaluated for that condition ($n = 5$). (a) Head scales and (b) tail scales.

Table 1
List of p-values for the repeated measures ANOVA performed to evaluate the differences in mechanical properties of the Internal Elasmodine (IE) specimens as a function of polar solvent conditioning. The responses are presented separately for results of the head and tail region. The symbols Ac, Ar, E, H and M represent the acetone, air, ethanol, HBSS and methanol conditions, respectively. Those boxes that are highlighted in bold are comparisons with no significant difference ($p > 0.05$).

Parameters	Region	p-values									
		H vs. M	H vs. E	H vs. Ac	H vs. Ar	M vs. E	M vs.Ac	M vs. Ar	E vs. Ac	E vs. Ar	Ac vs. Ar
Strength	Head	<0.05	<0.05	<0.05	<0.05	**0.64146**	<0.05	<0.05	<0.05	<0.05	<0.05
	Tail	<0.05	<0.05	<0.05	<0.05	**0.33362**	<0.05	<0.05	<0.05	<0.05	**0.07374**
Elastic modulus	Head	<0.05	<0.05	<0.05	<0.05	<0.05	<0.05	<0.05	<0.05	<0.05	<0.05
	Tail	<0.05	<0.05	<0.05	<0.05	<0.05	<0.05	<0.05	<0.05	<0.05	<0.05
Modulus of toughness	Head	<0.05	<0.05	<0.05	<0.05	**0.53792**	<0.05	<0.05	<0.05	<0.05	**0.7168**
	Tail	<0.05	<0.05	<0.05	<0.05	**0.60184**	<0.05	<0.05	<0.05	<0.05	**0.1313**
Failure strain	Head	<0.05	<0.05	<0.05	**0.21834**	**0.16458**	**0.13536**	<0.05	**0.55304**	<0.05	<0.05
	Tail	<0.05	<0.05	<0.05	**0.43007**	**0.11163**	**0.07599**	<0.05	**0.73298**	<0.05	<0.05

ondary region of linear strain hardening behavior. Note that this description implies mechanical behavior but not the mechanisms responsible. There is no connection to the process of dislocation pileup in metals; further description of the contributing mechanisms in fish scales is discussed later. The responses obtained from these two treatments exhibit very similar shape, with proportional limit/yield strains associated with the transition to strain hardening at approximately 1.5%. The mean yield strengths of the IE specimens from the head region evaluated in acetone and air are approximately 25 MPa and 40 MPa, respectively. These values are only slightly higher than those from the tail region, with values of 22 MPa and 35 MPa, respectively.

The mechanical properties obtained from the tensile tests on the IE specimens are summarized in Fig. 5. Specifically, the strength, elastic modulus, modulus of toughness and strain to failure are shown in Fig. 5a through 5d, respectively. Separate responses are shown for specimens from the head and tail scales for each condition. There is a significant increase ($p \leq 0.05$) in the strength, elastic modulus and modulus of toughness with decreasing polarity of the solvents, except for the methanol and ethanol whose polarities are similar. The strain to failure values in Fig. 5d exhibit an increase with decreasing polarity, with exception of the response for the HBSS treatment, which exhibits the lowest strain to failure of all conditions. The specimens evaluated in methanol achieved the largest strain to failure for scales from both the head and tail regions.

The mechanical properties of the IE specimens obtained from the head and tail regions are very similar overall ($p > 0.05$), but there are a few exceptions. Most noteworthy is the significantly larger ($p \leq 0.05$) elastic modulus of the IE specimens from the head region in acetone and air. The strain to failure of the head and tail scales have the opposite order, with larger values exhibited by the specimens of the tail for the methanol, ethanol and acetone solvents; the differences are nearing significance. A detailed description of the differences in mechanical properties between the treatments is presented in Table 1. There are significant differences in the properties of specimens between the majority of the polar solvents. However, significant differences between the methanol-soaked and ethanol-soaked samples are limited to the elastic modulus. Of all the mechanical properties evaluated, the lowest extent of significant differences caused by the polar solvent treatments is the strain to failure, which is also apparent in Fig. 5d.

The apparent Poisson's ratio (APR) of the IE specimens was estimated from the ratio of average transverse and axial strains measured within a central window of the gage section as shown in Fig. 6a. The history in APR as a function of the axial strain is shown for specimens of the head and tail regions in Fig. 6b and c, respectively. Similar to Fig. 4, the APR distributions are presented in terms of the moving average and standard deviation of all the specimens evaluated for that specific polar solvent treatment. An APR response for a polycarbonate (PC) specimen is also shown as a reference (control) in Fig. 6c; the evaluation was conducted in air and using the same loading conditions applied to the scales. Note that within the elastic range the Poisson's ratio for the PC control was 0.3, which is in very close agreement with that reported in the literature for this material [55–58]. After the onset of inelastic deformation, the APR value for the PC control ranges from roughly 0.3 to 0.45. The values obtained for the PC in both the elastic and inelastic range provide confidence in the estimated APR values for the IEs. The APR distributions for the head and tail regions are very similar with values range from 0 to nearly 2.5. That far exceeds the range in Poisson's ratio for isotropic materials that behave according to a continuum ($0 \leq \text{PR} \leq 0.5$). The APR increases with strain and exceeds 0.5 for all scale specimens maintained in a po-

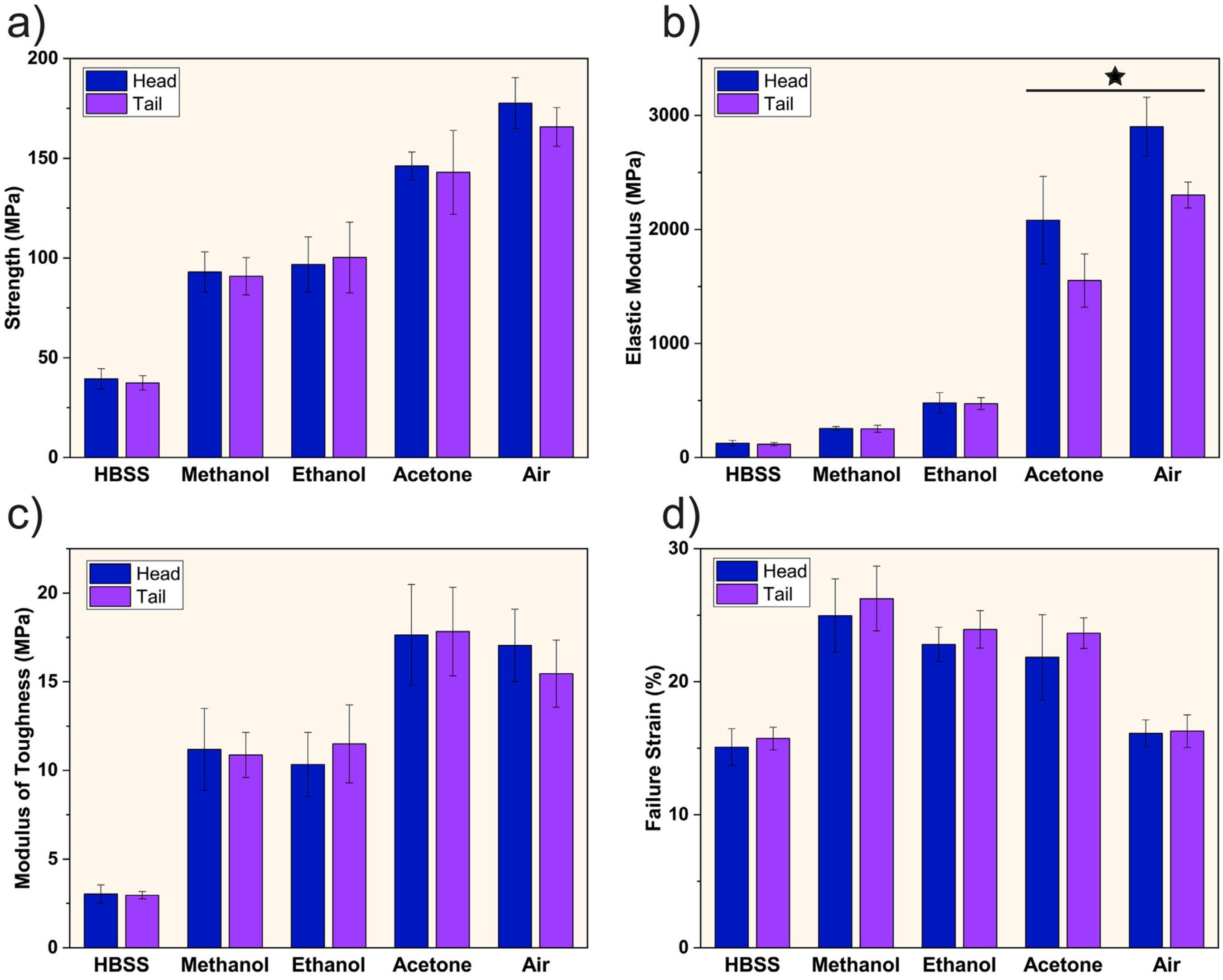

Fig. 5. Mechanical properties determined from the IE of scales from the head and tail regions as a function of the loading environment (treatments). (a) Tensile strength (S), (b) elastic modulus (E), (c) modulus of toughness (MOT) and (d) failure strain. The properties from the head and tail scales are not significantly different except for the values of E in the acetone and air-dried conditions (as highlighted in (b)). For these two treatments, the elastic modulus of the head and tail scales are significantly different ($p \le 0.05$), as indicated with a star.

lar solvent (HBSS, methanol, ethanol and acetone). The values for the acetone condition are the lowest of all solvents. Although the specimens evaluated in air as well as the PC specimens undergo an increase in APR with strain, they remain at APR ≤ 0.5, indicating that both behave as an isotropic continuum.

The distribution in APR curves with respect to the solvent polarity contrasts the order of the stress–strain responses obtained from the tensile tests. For instance, the APR values for the HBSS condition are the largest, whereas the stress–strain responses exhibit the lowest modulus and strength. Similarly, the acetone-treated and air-dried samples exhibit the lowest APR, remaining less than 0.6 overall, whereas the stress–strain responses in acetone and air exhibited the largest elastic modulus and strength. The APR responses for the specimens evaluated in HBSS, ethanol and methanol exhibit very similar characteristics, including a steep rise with increasing strain until reaching a plateau and/or failure in the case of ethanol. The APR responses of the specimens in HBSS and methanol decrease with further strain in both Fig. 6a and b. These differences are expected to be attributed to the contributions of interpeptide bonding and lubrication to the mechanisms of deformation, which require further discussion.

4. Discussion

Previous research concerning fish armors and their bioinspired derivatives has involved evaluations of the scales as well as the scales and underlying skin as a system [26,39–41]. These contributions have established that the scales act as the stiff protective phase, and they are partially embedded in a soft tissue, which renders flexibility. The combination of soft tissue and mineralized scale provides both flexibility and protection. However, elasmoid scales are thin and very flexible on their own, which is much different than ganoid scale structures. Thus, the elasmoid scales exhibit both of the important qualities reflected in “protecto-flexibility”, independent of the backing skin.

Previous studies concerning fish scales have established that the less mineralized plies of the elasmodine (i.e., the IE) are essential to various aspects of their mechanical behavior. Indeed, the capacity for inelastic deformation and large toughness of scales are a product of a combination of mechanisms that operate within this layer, including fibril sliding, fibril reorientation, and fibril stretching [15,20]. The individual plies (or lamellae) of the Bouligand structure adjust their orientation in response to the loading di-

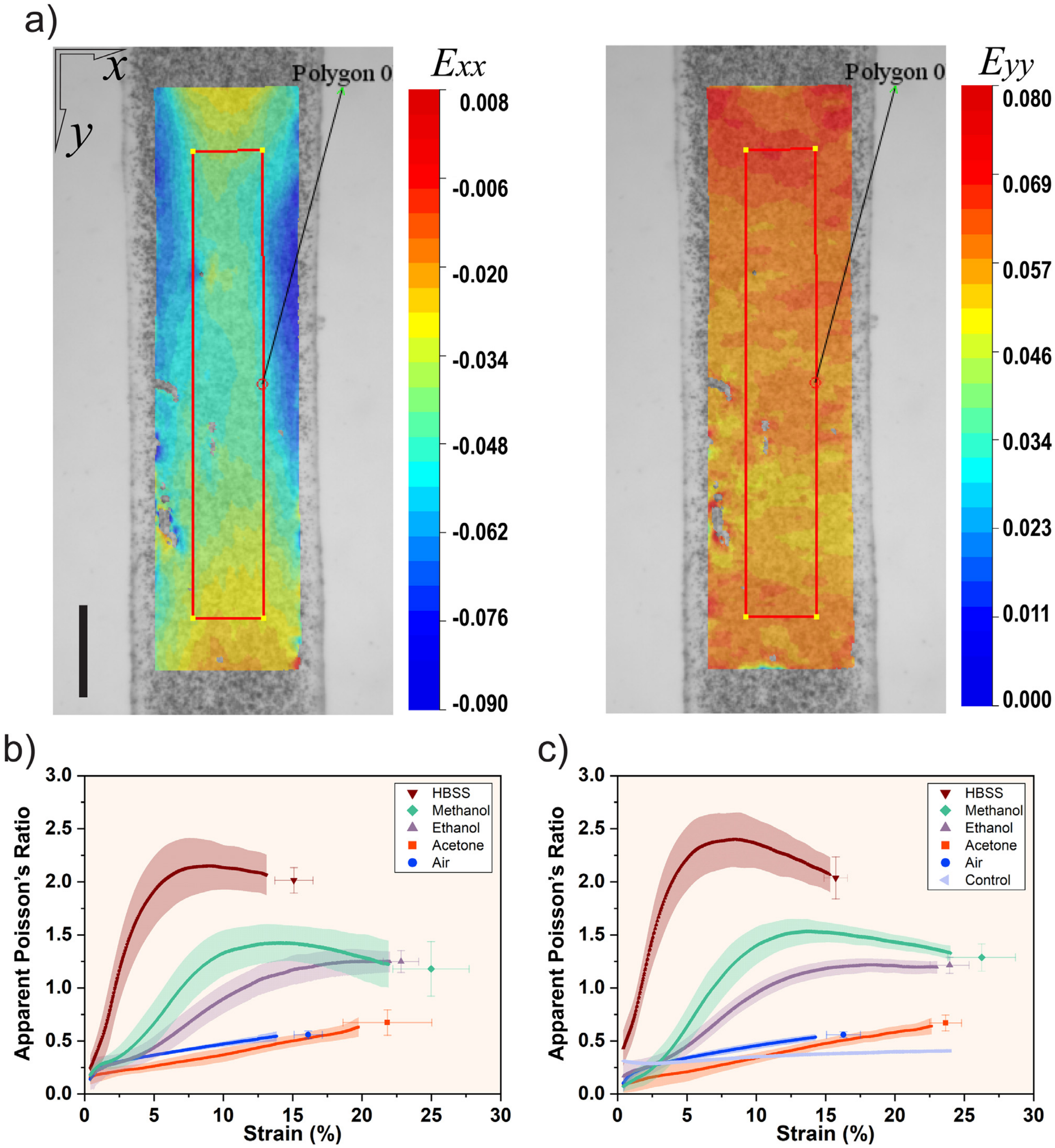

Fig. 6. Poisson's ratio distributions for the IE specimens as a function of strain and different treatments. (a) A region of interest in the gage section was selected (Polygon 0). Scale bar = 1 mm. The strain measurements for the axial (y) and transverse (x) directions were used to determine the apparent Poisson's ratio as a function of the axial strain for each treatment condition, and are shown for the (b) head scales, and (c) tail scales. The data in (b) and (c) represents the moving average and standard deviation of the Poisson's estimates obtained from all scales evaluated for that condition ($n = 5$). In (c), the control is polycarbonate.

rection, and as a function of the stacking sequence of the layers of collagen fibrils. Specifically, lamellae with fibril orientations close to the loading axis rotate towards the tensile direction, which is accompanied by stretching of the fibrils and interfacial sliding to adapt to this reorientation. The interplay between stretching and sliding is a function of intermolecular bonding and lubrication within and about the collagen fibrils. These factors regulate the resistance to molecular movements, which are also dependent on the degree of hydration and the contribution of the "water sheath". Indeed, the stiffness, strength and toughness of scales have been shown to depend on the level of hydration and water content [7,18,27,42].

Previous evaluations concerning the mechanical behavior of elasmoid scales obtained from different anatomical regions of carp identified that the properties varied from the head to the tail of the fish [27]. These spatial variations were interpreted to arise from differences in the degree of mineralization. The apatite is primarily limited to the LL in scales from the middle and tail regions, whereas in scales from the head region the mineral reinforcement extends to within the EE. After being subjected to an ethanol treatment, scales from the head region exhibited the maximum strength, toughness and elastic modulus of all regions evaluated, which was attributed to a combination of interfibril hydrogen bonding and the comparatively larger volume fraction of mineral reinforcement [27]. Notably, the largest change in mechanical properties with ethanol exposure occurred to scales of the tail, which was due to the lower interference of mineral to the interpeptide bonding in the presence of ethanol. That observation suggested that the mechanical behavior of these flexible armors could be tuned by modulating the interpeptide bonds and their effects on peptide and fibril interactions.

The mechanistic aspects of fibril reorientations in elasmoid scales and their contribution to the deformation behavior have become a topic of interest. Recently reported studies [2,27,43] describing the mechanical property changes in scales under dehydration provide some insight, but covered a limited range in solvent polarity. The large number of polar solvents used to treat the IE specimens in the present study is the key to advancing this knowledge.

Hoy's solubility parameter for hydrogen bonding (δ_h) is frequently used for describing the effectiveness of polar solvents to develop hydrogen-bonds within collagen fibrils. The H-bonds form preferentially between the collagen peptides, except within the presence of polar solvents that have higher affinity for hydrogen bonding, i.e. with δ_h values higher than that of the interpeptide bonds. Water (and HBSS) has a δ_h equal to 40.4 MPa$^{1/2}$, which is one of the solvents with the highest reported polarity. The δ_h for methanol, ethanol, and acetone are lower, with values of 24.0, 20.0, and 11.0 MPa$^{1/2}$, respectively. For relatively dry demineralized collagen of dentin, the δ_h value is postulated to be 14.8 MPa$^{1/2}$ [28]. Thus, when collagen fibrils are exposed to solvents with a δ_h < 14.8 MPa$^{1/2}$ (e.g., acetone) interpeptide H-bonds develop. However, when exposed to solvents with $\delta_h >$ 14.8 MPa$^{1/2}$ (i.e., HBSS, ethanol and methanol) hydrogen bonds develop preferentially between the interpeptide sites of the proteins and the solvent molecules that penetrate within the fibrils. These bonds interfere with the interpeptide hydrogen bonds between the protein molecules of the triple helix.

The aforementioned description provides a basis for understanding the effects of the polar solvents on the scale IE from a mechanistic perspective. In essence, the presence of water establishes a "sheath" that prevents the fibrils from forming interpeptide H-bonds. The solvent molecules serve to lubricate the peptide chains of the triple helix, which reduces the resistance to molecular movements and sliding between the collagen fibrils. This lubrication contributes at the fibril and lamellae level. On the other hand, the treatments consisting of acetone and air-drying enable the formation of interpeptide bonds between the collagen peptides in the plies of the elasmodine. Although the δ_h values for the air and acetone treatments are similar (14.8 and 11.0, respectively), the critical difference is the lubrication participating in those exposed to acetone via the solvent molecules that undergo hydrogen bonding with the proteins. This microstructural difference is the key to the differences in deformation behavior between the air and acetone treatment responses, in comparison to all others (ethanol, methanol and HBSS), which is distinctly evident in Figs. 4 and 6.

The term "strain-hardening" was applied to describe the secondary linear portion of the stress–strain curves for the acetone and air conditions and the prominent increase in resistance to deformation with increasing inelastic strain. While this term is often applied to characterize the response of metals, and is generally associated with dislocation pileup at grain boundaries and other obstacles, the terminology used for the scales certainly does not imply the same mechanisms. The secondary linear portion of these two treatments with $\delta_h \leq$ 14.8 MPa$^{1/2}$ is associated with the increased resistance to fibril sliding and ply reorientation, which results from the increasing extent of interpeptide bonding. The APR distributions in Fig. 6 show that the degree of ply and fibril reorientation is substantially decreased in these two conditions, particularly in air, which is also due to the absence of a liquid lubricant and larger extent of molecular and fibril friction. That further reduces the interfacial sliding, which is active in the presence of higher polarity solvents. As such, the axial elongation in the scales subjected to air and acetone is attributed to elongation of the fibrils themselves. While that process renders an increase in strength it does not suffer the common penalty, which is a decrease in ductility. The strain to failure of scales in the acetone and air conditions is comparable to that in HBSS. That appears to be another benefit of the increase in the extent of interfibril bonding, which resists the development and progression of interfacial damage associated with sliding between fibrils and plies, which are the preludes to fracture. The slightly lower ductility in air appears to result from the absence of the water sheath and its contribution to a reduction in the permissible fibril elongations to failure.

Reviewing the stress–strain responses in Fig. 4, the strength and elastic modulus of the scales increases with decrease in δ_h value of the solvent they were exposed to. When the IE specimens are placed within a solvent with a weaker bonding ability than water, the water molecules in and between collagen proteins are displaced, which allows the formation of direct bonding between adjacent peptide chains. Furthermore, the extent of interpeptide bond formation depends on the magnitude of δ_h; the lower the value of δ_h, the greater propensity for their formation, which suggests that there are more interpeptide bonds formed in the IEs exposed to a solvent with lower δ_h value. Hence, when the IEs are exposed to ethanol and methanol, a portion of interpeptide H-bonds are formed as well as some bonds between the ethanol (methanol) and collagen chains. The δ_h value for these solvents is close to 14.8 MPa$^{1/2}$, which allows the coexistence of these two H-bonds. However, in the presence of acetone with lower δ_h value, a greater number of interpeptide bonds develop, thereby increasing the resistance to interfibrillar sliding, which fosters an increase in resistance to both elastic and inelastic deformation at the macroscopic level [27].

After exposure to the polar solvents, the mechanical properties of the IE specimens underwent significant changes (Table 1 and Fig. 5). Moreover, the extent of change with respect to water is directly related to the solvent polarity (δ_h). Those specimens exposed to acetone with lowest δ_h exhibited the highest elastic modulus, as well as the largest strength and modulus of toughness, which is a result of the direct interpeptide bonding. Conversely, in HBSS the specimens exhibited the lowest elastic modulus, strength and MOT due to contributions of the "water sheath" as a lubricant that facilitates interfibrillar sliding. The difference in these properties between the IE specimens of the head and tail regions result from the larger degree of residual mineralization in scales from the head region [8,27]. In the solvent treatments with low polarity ($\delta_h \leq$ 14.8 MPa$^{1/2}$), the IEs of the head are significantly stiffer than those from the tail region (Fig. 5c). We believe that the increase in interpeptide hydrogen bonds restricts the contribution of interfibrillar sliding, which magnifies the effect of mineral crystals on the elastic modulus of the IEs. This occurs from the dimensional shrinkage of the tissue, which locks the mineral crystals embodied within the collagen, and the transition to continuum behavior. The elastic modulus of the mineral phase is more than an order of magnitude higher than that of collagen. Adding nanoscopic hydroxyapatite platelets is critical to increase the stiffness of collagen fibrils [44]. The greater physical coupling between the mineral platelets and fibrils increases their contribution to stiffening.

Contrary to the reduction in strain to failure of bone with dehydration [45], the IE of the scales retained its ductility with dehydration (Fig. 5d), which is consistent with the responses of other biological tissues such as skin [46,47] and tendons [48]. In bone, the interfibrillar spaces are largely occupied by mineral crystals [12], which interferes with the formation of interpeptide bonds during dehydration. That is a key difference between the scales and bone. Owing to the negligible mineral content of the IEs, more interpeptide H-bonds develop at the interfaces of the fibrils during dehydration, which increases interfacial strength. The strong interfacial adhesion increases the proportion of fibril elongation in the deformation, which primarily consists of interfibrillar/interlamellar sliding and fibril elongation, during stretching, preserving or even improving the ductility of the dehydrated IEs. Akin to bone [49,50], even slight variations in mineral content of the IEs can contribute to the strain to fracture. The slightly larger mineral content of the IE in scales from the head region [27] results in lower strain to failure as shown in Fig. 5d. Although skin and tendon have quite different microstructure from that of the scales, it appears that the absence of mineral is responsible for the retention of ductility with dehydration, and that it arises from the increase in interfibrillar bonding.

The changes in mechanical behavior characterized by the tension tests are not sufficient to fully understand the relative contributions of fibril sliding and reorientations to the scale mechanics. Here is the important value of the APR distributions (Fig. 6) in understanding the mechanisms contributing to deformation. A schematic description for deformation within an isolated circular element of the elasmodine is shown in Fig. 7a, which was motivated by *in situ* small-angle X-ray diffraction measurements [15,20,51]. The collagen fibrils within each lamella undergo a combination of elongation and reorientation to angles more coincident with the tensile axis. Disregarding elongation, fibril rotation towards the tensile axis involves interfibrillar sliding, as shown schematically in Fig. 7b. This rotation depends on the extent of lubrication provided by the “water-sheath” established by the polar solvent, as well as the resistance from intermolecular hydrogen bonding. Decoupling the fibril elongation and rotation, a fibril reorientation of ϕ is accompanied with a relative longitudinal elongation from S_0 to S_1. The fibril reorientation is superposed with local axial elongation as shown in Fig. 7c. This model can be used to develop a simple analytical expression for the APR as a function of fibril reorientations. At the level of the lamellae, the axial strain associated with the change in projected length of the fibrils when it rotates from some initial angle Φ_0 to Φ_1 can be expressed as

$$e_{yy} = \frac{(L + \Delta L) \cdot \sin \Phi_1 - L \cdot \sin \Phi_0}{L \cdot \sin \Phi_0} \tag{1}$$

where L denotes the initial length of the fibril and ΔL is the elongation. The corresponding transverse strain (in the x-direction) is given by

$$e_{xx} = \frac{(L + \Delta L)\Delta \cos \Phi_1 - L \cdot \cos \Phi_0}{L \cdot \cos \Phi_0} \tag{2}$$

Combining Eqs. (1) and (2), the apparent Poisson’s ratio associated with this rotation (APR_{rot}) can be described by

$$APR_{rot} = -\frac{e_{xx}}{e_{yy}} = \tan \Phi_0 \cdot \frac{L \cdot \cos \Phi_0 - (L + \Delta L) \cdot \cos \Phi_1}{(L + \Delta L) \cdot \sin \Phi_1 - L \cdot \sin \Phi_0} \tag{3}$$

The relative effects of fibril rotations on the APR distributions of the IE specimens can be interpreted with help of Eq. (3), as well as contributions from the various solvents to these distributions. In adopting this model, it is necessary to choose an initial fibril orientation (Φ_0) relative to the direction of axial loading. For the case where the fibril undergoes rotation/reorientation from $\Phi_0 = 45^\circ$ towards the tensile axis ($\Phi_0 = 90^\circ$) and the contribution of elongation is negligible ($\Delta L = 0$), APR $= APR_{rot}$ and the distribution in APR as a function of axial strain is shown in Fig. 7d. If a simple functional relationship is assumed that couples the rotation and the axial elongation over an increasing extent of elongation, the APR evolves with axial elongation as shown in Fig. 7d. Admittedly, these curves are not in perfect agreement with the shape of the APR distributions in Fig. 6b and c and it easy to understand why. The treatment in Fig. 7d applies to a single uniform fibril offset angle, whereas the IE specimens consist of an array of orientations through the thickness ($0 \leq \Phi_0 \leq 90^\circ$). In addition, the contribution of axial elongation is dependent on the relative stiffness and strength of the “interfibrillar-linkers”, as described by Ahmadzadeh et al. [52], which controls the onset of sliding. There is a point where the fibrils begin to unravel and axial elongation takes over, which is a third mechanism of deformation.

The simple analytical treatment of ply rotations provides one aspect of justification for the large APR value of the IE for HBSS, methanol and ethanol. Previous experimental investigations on soft tissues have reported APR values in the same range as those received for the IE of the scales, including that reported for the ligament of human hip joints (1.65 ± 0.35) [53] and for the sheep flexor tendon (2.98 ± 2.59) [54]. As fibril elongation becomes a greater part of the deformation response (increasing ΔL) of the IE, the APR distributions become more shallow with axial strain. Clearly the interfibrillar-sliding associated with fibril reorientation is the primary contribution to the variation in APR within the HBSS environment. This is attributed to the “lubrication” provided by the water sheath and the limited interpeptide bonding within the fibrils. Conversely, the APR curves of the acetone-soaked IEs is the lowest in both Fig. 6a and b (ignoring the PC control). That behavior implies that interfibrillar sliding is restrained, which agrees with the explanation of the interpeptide H-bond formation elicited by the absence of water.

There is an additional consideration of fibril reorientations that occur within extracted tensile specimens, the measured mechanical properties, and how well they reflect the “true” mechanical properties of the whole scale. The reorientation of fibrils within the off-axis plies could depend on two factors, namely the length of the fibrils and its contributions to the frictional resistance to interfacial sliding, as well as the uniformity of the fibril orientation over the entire scale width. Narrow tensile specimens will have less resistance to reorientation and more uniform ply orientations across the specimen width than those that are wider. That may pose some difficulty in comparing the mechanical properties of scales from investigations that have used different tensile specimen dimensions. Nevertheless, the objective of the present study was to understand the role of water to interfibrillar lubrication and sliding, and the specimen dimensions were consistent for all of the specimens and polar solvent treatments. It may be worthwhile in future evaluations of fibril reorientation to consider the importance of specimen width.

The APR curves for the HBSS and methanol conditions in Fig. 6b and c exhibit a plateau, followed by a reduction in the APR with further axial strain. That behavior is hypothesized to result from a transition from the fibril reorientation to the stretching mechanisms. For these high polarity solvents, the more prominent liquid sheath facilitates interfibrillar sliding preferentially, and to the greatest extent for the HBSS. The plateau in the APR curves reflects a saturation in the reorientation mechanism, after which elongation of the fibrils ensues. A reduction in the transverse deformation with axial strain follows and results in a decrease in the APR. Of course, this is coupled with fibril pullout and failure, which also play an increasingly important role in the deformation process at large strains. Responses for the acetone and air condition in Fig. 6 exhibit a single trend, reflecting that fibril reorientation assisted by interfibrillar sliding was restrained by the higher degree of interpeptide hydrogen bonding.

To complement the experimental results for the APR of the fish scales, the deformation response of a fibrous laminated ultra-

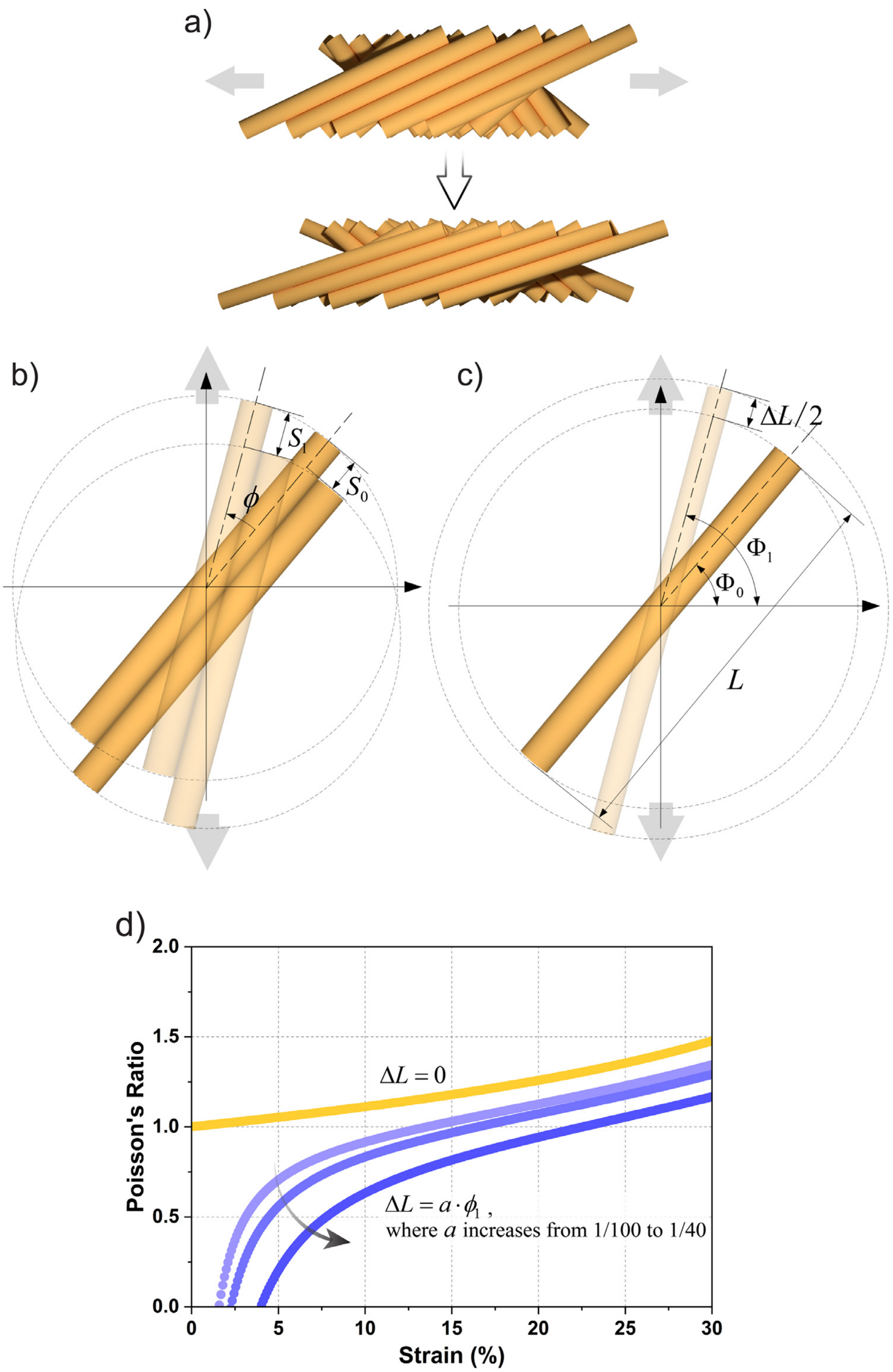

Fig. 7. Sliding mechanics associated with deformation of the scales during tension. (a) The collagen fibril plies of the Bouligand structure rotate to align with the loading direction, which involves sliding and elongation of the fibrils. (b) The "off"-axis" plies of collagen fibrils undergo rotation towards the tensile axis. This process involves shear, rotational interfibrillar sliding and axial deformation. The sliding and rotation are resisted by interpeptide bonding and assisted by intermolecular lubrication. A rotation ϕ causes an axial displacement that evolves between two neighboring fibrils from S_0 to S_1. (c) The deformation mechanism from the perspective of a single fibril. With rotation from Φ_0 to Φ_1 the fibril with an original length of L undergoes an elongation of ΔL. (d) Contributions of rotation and elongation components on the APR according to Eq. (3).

high molecular weight polyethylene (UHMWPE; DSM Dyneema^{TM} HB26) was evaluated in uniaxial tension. The material has a microstructure similar to the IE of the scales. The sheet consists of four orthogonal plies of UHMWPE fibers with interface matrix of low stiffness polyurethane (PUR) elastomer. Tensile specimens were sectioned from the laminate with an angle of 45° between the orientation of the fibers in each ply and the longitudinal axis (Fig. 8a). The fibers are large enough (~17µm) to be observed by an industrial camera with a microscope lens. The axial and transverse strains resulting from uniaxial tension were obtained by DIC and

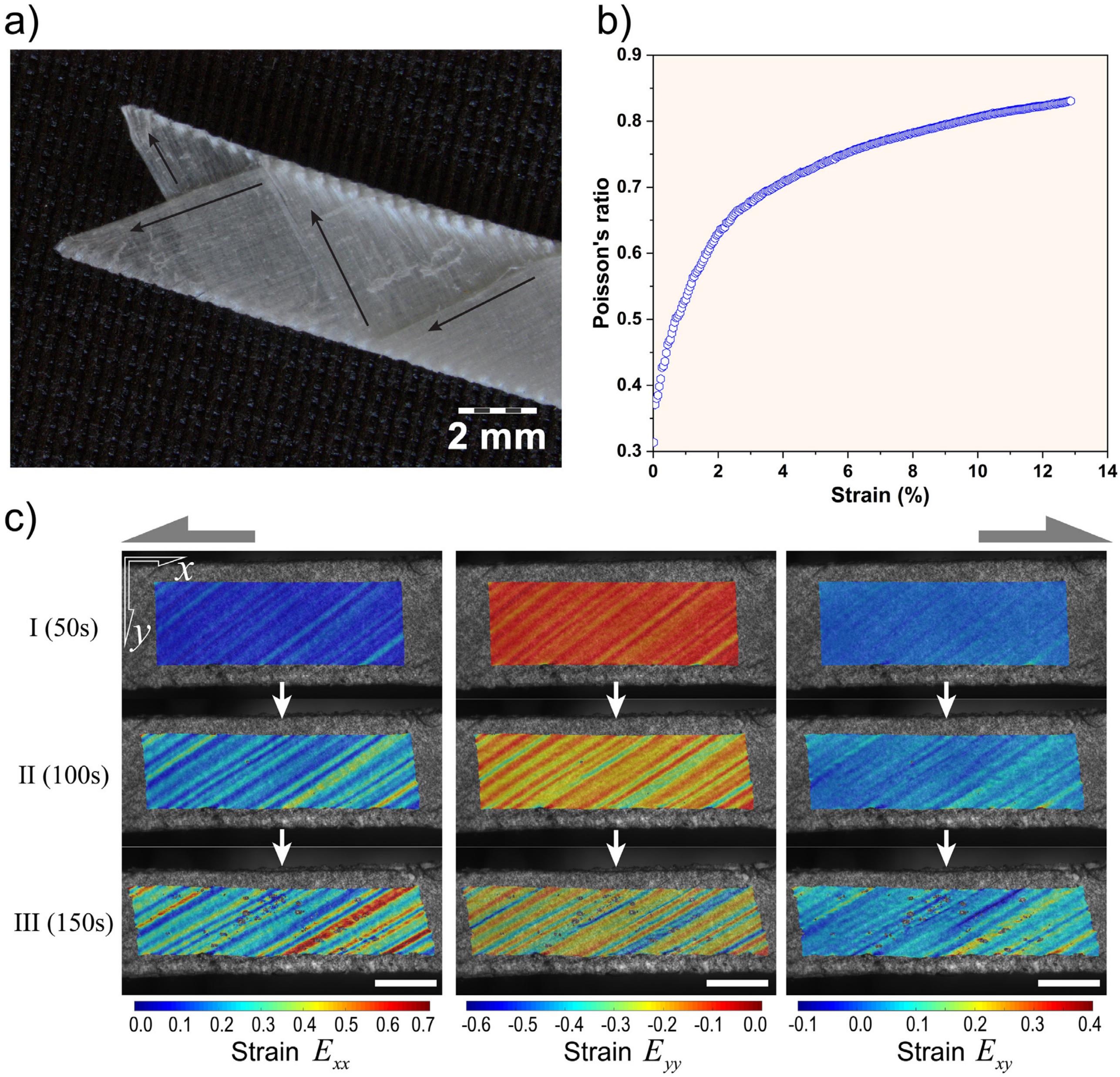

Fig. 8. Uniaxial tensile test performed on a cross-ply laminate of to provide additional understanding of the results for the scales. The Dyneema^{TM} has a similar structure to the IE of the fish scales. (a) The cross-ply structure of a UHMWPE specimen, which was prepared with fiber orientations of ± 45° to the axial direction of the specimen. (b) A typical Poisson's ratio evolution for the Dyneema^{TM} under elongation. (c) The full-field strain maps obtained through the 2D-DIC during tensile testing. Scale bar = 1 mm.

used to evaluate the APR response over the range of axial strain to failure. The APR response with axial strain is shown in Fig. 8b and is very consistent with that for the IEs exposed to ethanol shown in Fig. 6b and c. Strain maps within a sample corresponding to the longitudinal, transverse and shear components are shown in Fig. 8c. The evolution in the e_{xx} and e_{yy} maps and the e_{xy} maps show the fiber reorientation with increasing axial strain as enabled by interfibrillar sliding. These responses emphasize that the unique mechanical properties of the IEs are a function of the fibril arrangement, as well as the mechanistic contribution of the water environment to the interfibrillar lubrication. Although these synthetic materials can be prepared with any lamination pattern desired, the remaining challenge is identifying how to actively control the interbrillar bonding and lubrication.

The dramatic change in deformation characteristics of the scales activated by the solvents and the interplay between interpeptide bonding and molecular lubrication is remarkable. It is arguably one of the most interesting aspects of these natural armor materials. Despite the novelty of the findings, there are some limitations to this investigation. For example, the strength of the hydrogen bonds contributing to the changes in the scale mechanics were not measured. As previously highlighted, the relative contributions of interfibrillar sliding and fibril rotation may depend on the free length of the fibers (i.e., the width of the specimens) and that was not considered in the present investigation. Another limitation is that the scale properties were evaluated at a single strain rate and the relative contribution of interpeptide bonds is a function of strain rate [2]. Future studies could address the changes in contributing mechanisms as a function of strain rate. Another limitation relates to the relative importance of the scale lamination patterns to the deformation responses. The lamination patterns and other aspects of the morphology are unique among different fish species [17] and are undoubtedly important to the interplay between interfibrillar sliding (assisting reorientation) and fibril elongation. That topic is reserved for future studies. Nevertheless, the findings of this investigation make a unique contribution – they provide a detailed mechanistic description of the role of intermolecular bonding and lubrication on the unique mechanical behavior of fish scales. Future efforts to develop next-generation flexible materials for protection could benefit from harnessing this unique capability.

5. Conclusion

An experimental investigation of contributions from intermolecular lubrication and intermolecular bonds to the mechanisms of deformation in scales obtained from the head and tail regions of the Black Carp was performed. Specimens consisting of the internal elasmodine were subjected to tensile loading to failure within selected polar solvents ranging from HBSS to acetone. According to results of this investigation, the following conclusions are drawn:

(i) The elastic modulus, strength and toughness of the IE of the scales increased significantly with decreasing Hoy's solubility parameter of the solvent treatments. The elastic modulus increased up to 30x, with regards to that value in HBSS, and the strength and modulus of toughness increased up to 4x and 5x, respectively.

(ii) There were no significant differences in the mechanical properties between head and tail scales in regards to the effects of the polar solvents on the strength, toughness and strain to failure. However, in both the acetone and air environments the elastic modulus was significantly larger in the scales of the head region. This difference is expected to result from a greater degree of mineralization and its contribution to the elastic responses.

(iii) In HBSS, the apparent Poisson's ratio increased with axial loading from 0.2 to a maximum of nearly 2.4. The large value corresponds to the extent of fibril rotation and sliding that accompanies the deformation process. The range in apparent Poisson's ratio with axial strain was reduced with exposure to the polar solvents and decreased with decreasing polarity of the solvent.

(iv) Dehydration in air, which results in more extensive interpeptide bonding and removes the intermolecular lubricant resulted in the highest elastic modulus and strength, but lower strain to failure than that of the polar solvents.

Declaration of Competing Interest

The authors have no conflicts to declare.

Acknowledgments

This investigation was supported in part by the National Science Foundation of China (NSFC #11872240: PI D. Arola, #11772092 and 11472081: PI F. Yang), the China Scholarship Council (CSC #201706090091: H. Jiang) and the Postgraduate Research & Practice Innovation Program of Jiangsu Province (KYCX17_0053). The authors are grateful for the insight and advice given by Dr. Xiaoyuan He and Dr. Xinxing Shao (Department of Mechanics, Southeast University, China), whose experiences with digital image correlation led to important improvements to the methods that were applied in this investigation. Their help was crucial to the success of this project.

References

[1] D. Zhu, C.F. Ortega, R. Motamedi, L. Szewciw, F. Vernerey, F. Barthelat, Structure and mechanical performance of a "modern" fish scale, Adv. Eng. Mater. 14 (4) (2012) B185–B194.
[2] D. Arola, S. Ghods, C. Son, S. Murcia, E.A. Ossa, Interfibril hydrogen bonding improves the strain-rate response of natural armour, J. R. Soc. Interface 16 (150) (2019) 20180775.
[3] J. Bereiter-Hahn, L. Zylberberg, Regeneration of teleost fish scale, Comp. Biochem. Physiol. B 105 (4) (1993) 625–641.
[4] M. Seeley, N. Miller, B. Walther, High resolution profiles of elements in Atlantic tarpon (megalops atlanticus) scales obtained via cross-sectioning and laser ablation ICP-MS: a literature survey and novel approach for scale analyses, Environ. Biol. Fishes 98 (11) (2015) 2223–2238.
[5] W. Liu, Y. Zhang, G. Li, Y. Miao, X. Wu, Structure and composition of teleost scales from snakehead channa argus (cantor)(perciformes: channidae), J. Fish Biol. 72 (4) (2008) 1055–1067.
[6] D. Arola, S. Murcia, M. Stossel, R. Pahuja, T. Linley, A. Devaraj, M. Ramulu, E.A. Ossa, J. Wang, The limiting layer of fish scales: structure and properties, Acta Biomater. 67 (2018) 319–330.
[7] A. Marino Cugno Garrano, G. La Rosa, D. Zhang, L.N. Niu, F.R. Tay, H. Majd, D. Arola, On the mechanical behavior of scales from cyprinus carpio, J. Mech. Behav. Biomed. Mater. 7 (2012) 17–29.
[8] M.J. Buehler, Molecular nanomechanics of nascent bone: fibrillar toughening by mineralization, Nanotechnology 18 (29) (2007) 295102.
[9] F.G. Torres, O.P. Troncoso, J. Nakamatsu, C.J. Grande, C.M. Gomez, Characterization of the nanocomposite laminate structure occurring in fish scales from arapaima gigas, Mater. Sci. Eng. C 28 (8) (2008) 1276–1283.
[10] S. Nikolov, M. Petrov, L. Lymperakis, M. Friak, C. Sachs, H.O. Fabritius, D. Raabe, J. Neugebauer, Revealing the design principles of high-performance biological composites using ab initio and multiscale simulations: the example of lobster cuticle, Adv. Mater. 22 (4) (2010) 519–526.
[11] A. Gautieri, S. Vesentini, A. Redaelli, M.J. Buehler, Hierarchical structure and nanomechanics of collagen microfibrils from the atomistic scale up, Nano Lett. 11 (2) (2011) 757–766.
[12] F. Barthelat, Z. Yin, M.J. Buehler, Structure and mechanics of interfaces in biological materials, Nat. Rev. Mater. 1 (4) (2016) 16007.
[13] M.M. Giraud, J. Castanet, F.J. Meunier, Y. Bouligand, The fibrous structure of coelacanth scales: a twisted 'plywood', Tissue Cell 10 (4) (1978) 671–686.
[14] A. Khayer Dastjerdi, F. Barthelat, Teleost fish scales amongst the toughest collagenous materials, J. Mech. Behav. Biomed. Mater. 52 (2015) 95–107.
[15] H. Quan, W. Yang, E. Schaible, R.O. Ritchie, M.A. Meyers, Novel defense mechanisms in the armor of the scales of the "living fossil" coelacanth fish, Adv. Funct. Mater. 28 (46) (2018) 1804237.
[16] V.R. Sherman, H. Quan, W. Yang, R.O. Ritchie, M.A. Meyers, A comparative study of piscine defense: the scales of arapaima gigas, latimeria chalumnae and atractosteus spatula, J. Mech. Behav. Biomed. Mater. 73 (2017) 1–16.
[17] S. Murcia, E. Lavoie, T. Linley, A. Devaraj, E.A. Ossa, D. Arola, The natural armors of fish: a comparison of the lamination pattern and structure of scales, J. Mech. Behav. Biomed. Mater. 73 (2017) 17–27.
[18] Y.S. Lin, C.T. Wei, E.A. Olevsky, M.A. Meyers, Mechanical properties and the laminate structure of arapaima gigas scales, J. Mech. Behav. Biomed. Mater. 4 (7) (2011) 1145–1156.
[19] M.A. Meyers, Y.S. Lin, E.A. Olevsky, P.Y. Chen, Battle in the amazon: arapaima versus piranha, Adv. Eng. Mater. 14 (5) (2012) B279–B288.
[20] E.A. Zimmermann, B. Gludovatz, E. Schaible, N.K. Dave, W. Yang, M.A. Meyers, R.O. Ritchie, Mechanical adaptability of the bouligand-type structure in natural dermal armour, Nat. Commun. 4 (2013) 2634.
[21] Z. Jia, Y. Yu, S. Hou, L. Wang, Biomimetic architected materials with improved dynamic performance, J. Mech. Phys. Solids 125 (2019) 178–197.
[22] Z. Yin, A. Dastjerdi, F. Barthelat, Tough and deformable glasses with bioinspired cross-ply architectures, Acta Biomater. 75 (2018) 439–450.
[23] E. Lin, Y. Li, C. Ortiz, M.C. Boyce, 3d printed, bio-inspired prototypes and analytical models for structured suture interfaces with geometrically-tuned deformation and failure behavior, J. Mech. Phys. Solids 73 (2014) 166–182.
[24] R. Lemanis, I. Zlotnikov, Finite element analysis as a method to study molluscan shell mechanics, Adv. Eng. Mater. 20 (3) (2018) 1700939.
[25] M.Q. Chandler, P.G. Allison, R.I. Rodriguez, R.D. Moser, A.J. Kennedy, Finite element modeling of multilayered structures of fish scales, J. Mech. Behav. Biomed. Mater. 40 (2014) 375–389.
[26] F.J. Vernerey, K. Musiket, F. Barthelat, Mechanics of fish skin: a computational approach for bio-inspired flexible composites, Int. J. Solids Struct. 51 (1) (2014) 274–283.
[27] S. Murcia, G. Li, M. Yahyazadehfar, M. Sasser, A. Ossa, D. Arola, Effects of polar solvents on the mechanical behavior of fish scales, Mater. Sci. Eng. C Mater. Biol. Appl. 61 (2016) 23–31.
[28] D.H. Pashley, F.R. Tay, R.M. Carvalho, F.A. Rueggeberg, K.A. Agee, M. Carrilho, A. Donnelly, F. García-Godoy, From dry bonding to water-wet bonding to ethanol-wet bonding. A review of the interactions between dentin matrix and solvated resins using a macromodel of the hybrid layer, Am. J. Dent. 20 (1) (2007) 7–21.
[29] V.K. Kinra, V. Dayal, Acoustic methods of evaluating elastic properties or, will the real young's modulus please stand up? in: Manual on Experimental Methods for Mechanical Testing of Composites, Springer, 1989, pp. 97–103.
[30] X. Dai, H. Yun, X. Shao, Y. Wang, D. Zhang, F. Yang, X. He, Thermal residual stress evaluation based on phase-shift lateral shearing interferometry, Opt. Laser Eng. 105 (2018) 182–187.
[31] J. Soons, P. Lava, D. Debruyne, J. Dirckx, Full-field optical deformation measurement in biomechanics: digital speckle pattern interferometry and 3d digital image correlation applied to bird beaks, J. Mech. Behav. Biomed. Mater. 14 (2012) 186–191.

[32] Z. Chen, B. Nadeau, K. Yu, X. Shao, X. He, M.C. Goh, A. Kishen, Whole-field macro- and micro-deformation characteristic of unbound water-loss in dentin hard tissue, J. Biophotonics 11 (9) (2018) e201700368.
[33] T. Yuan, X. Dai, X. Shao, Z. Zu, X. Cheng, F. Yang, X. He, Dual-biprism-based digital image correlation for defect detection of pipelines, Opt. Eng. 58 (1) (2019) 014107.
[34] J.P. Carey, Handbook of Advances in Braided Composite Materials: Theory, Production, Testing and Applications, Woodhead Publishing, 2016.
[35] A. Pissarenko, W. Yang, H. Quan, K.A. Brown, A. Williams, W.G. Proud, M.A. Meyers, Tensile behavior and structural characterization of pig dermis, Acta Biomater. 86 (2019) 77–95.
[36] X. Shao, Z. Chen, X. Dai, X. He, Camera array-based digital image correlation for high-resolution strain measurement, Rev. Sci. Instrum. 89 (10) (2018) 105110.
[37] X. Shao, X. Dai, X. He, Noise robustness and parallel computation of the inverse compositional Gauss–Newton algorithm in digital image correlation, Opt. Laser Eng. 71 (2015) 9–19.
[38] M.A. Sutton, J.J. Orteu, H. Schreier, Image Correlation For Shape, Motion and Deformation Measurements: Basic Concepts, Theory and Applications, Springer Science & Business Media, 2009.
[39] A. Browning, C. Ortiz, M.C. Boyce, Mechanics of composite elasmoid fish scale assemblies and their bioinspired analogues, J. Mech. Behav. Biomed. Mater. 19 (2013) 75–86.
[40] S. Varshney, J. Song, Y. Li, M.C. Boyce, C. Ortiz, Morphometric structural diversity of a natural armor assembly investigated by 2d continuum strain analysis, J. Struct. Biol. 192 (3) (2015) 487–499.
[41] S. Rudykh, C. Ortiz, M.C. Boyce, Flexibility and protection by design: imbricated hybrid microstructures of bio-inspired armor, Soft Matter 11 (13) (2015) 2547–2554.
[42] M.A. Meyers, A.Y.M. Lin, Y. Seki, P.Y. Chen, B.K. Kad, S. Bodde, Structural biological composites: an overview, JOM 58 (7) (2006) 35–41.
[43] A. Gautieri, M.I. Pate, S. Vesentini, A. Redaelli, M.J. Buehler, Hydration and distance dependence of intermolecular shearing between collagen molecules in a model microfibril, J. Biomech. 45 (12) (2012) 2079–2083.
[44] M.E. Launey, M.J. Buehler, R.O. Ritchie, On the mechanistic origins of toughness in bone, Annu. Rev. Mater. Res. 40 (1) (2010) 25–53.
[45] J. Samuel, D. Sinha, J.C.-G. Zhao, X. Wang, Water residing in small ultrastructural spaces plays a critical role in the mechanical behavior of bone, Bone 59 (2014) 199–206.
[46] W. Yang, V.R. Sherman, B. Gludovatz, E. Schaible, P. Stewart, R.O. Ritchie, M.A. Meyers, On the tear resistance of skin, Nat. Commun. 6 (2015) 6649.
[47] J. Ankersen, A.E. Birkbeck, R.D. Thomson, P. Vanezis, Puncture resistance and tensile strength of skin simulants, Proc. Inst. Mech. Eng. H 213 (6) (1999) 493–501.
[48] Y.P. Kato, D.L. Christiansen, R.A. Hahn, S.-J. Shieh, J.D. Goldstein, F.H. Silver, Mechanical properties of collagen fibres: a comparison of reconstituted and rat tail tendon fibres, Biomaterials 10 (1) (1989) 38–42.
[49] E. Novitskaya, P.Y. Chen, S. Lee, A. Castro-Cesena, G. Hirata, V.A. Lubarda, J. McKittrick, Anisotropy in the compressive mechanical properties of bovine cortical bone and the mineral and protein constituents, Acta Biomater. 7 (8) (2011) 3170–3177.
[50] S.P. Kotha, N. Guzelsu, Tensile behavior of cortical bone: dependence of organic matrix material properties on bone mineral content, J. Biomech. 40 (1) (2007) 36–45.
[51] W. Yang, V.R. Sherman, B. Gludovatz, M. Mackey, E.A. Zimmermann, E.H. Chang, E. Schaible, Z. Qin, M.J. Buehler, R.O. Ritchie, M.A. Meyers, Protective role of arapaima gigas fish scales: structure and mechanical behavior, Acta Biomater. 10 (8) (2014) 3599–3614.
[52] H. Ahmadzadeh, B.R. Freedman, B.K. Connizzo, L.J. Soslowsky, V.B. Shenoy, Micromechanical poroelastic finite element and shear-lag models of tendon predict large strain dependent Poisson's ratios and fluid expulsion under tensile loading, Acta Biomater. 22 (2015) 83–91.
[53] J. Hewitt, F. Guilak, R. Glisson, T.P. Vail, Regional material properties of the human hip joint capsule ligaments, J. Orthop. Res. 19 (3) (2001) 359–364.
[54] S.P. Reese, J.A. Weiss, Tendon fascicles exhibit a linear correlation between Poisson's ratio and force during uniaxial stress relaxation, J. Biomech. Eng. 135 (3) (2013) 034501.
[55] J.M. Whitney, in: Composite Materials: Testing and Design (Seventh Conference): A Conference, ASTM International, Philadelphia, 1986, pp. 2–4. April 1984.
[56] H. Krbecek, J. Krüger, M. Pietralla, Poisson ratios and upper bounds of intrinsic birefringence from Brillouin scattering of oriented polymers, J. Polym. Sci. Part B Polym. Phys. 31 (11) (1993) 1477–1485.
[57] J. Brandrup, E. Immergut, E. Grulke, Polymer Handbook, John Wiley & Sons Inc, New York, 1975.
[58] C. Pappalettere, Annealing polycarbonate sheets, Strain 20 (4) (1984) 179–180.